Available online at www.sciencedirect.com

ScienceDirect

Ceramics International 40 (2014) 1843–1850

CERAMICS INTERNATIONAL

www.elsevier.com/locate/ceramint

Comparison of thermo-mechanical characteristics of non-doped and 3 mol% B-site Zr-doped $Ba_{0.5}Sr_{0.5}Co_{0.8}Fe_{0.2}O_{3-\delta}$

G. Pećanac[a,*], L. Kiesel[b], R. Kriegel[b], J. Malzbender[a]

[a]Forschungszentrum Jülich GmbH, IEK-2, 52425 Jülich, Germany
[b]Fraunhofer Institute for Ceramic Technologies and Systems IKTS, Marie-Curie-Str. 17, 07623 Hermsdorf, Germany

Received 29 April 2013; received in revised form 4 July 2013; accepted 17 July 2013
Available online 25 July 2013

Abstract

A dense membrane layer supported by a thick porous substrate is a favorable design for advanced oxygen separation units used in Oxy-fuel processes and membrane reactors. Based on the highest permeation rates verified so far, $Ba_{0.5}Sr_{0.5}Co_{0.8}Fe_{0.2}O_{3-\delta}$ appears to be the most promising membrane and substrate material. This material, however, suffers from partial decomposition of cubic structure to hexagonal polymorphs at ~825 °C, which is associated with a significant oxygen permeation drop. The partial substitution of the B-site with 3 mol% zirconium has been suggested as one of solutions for suppressing this transformation. The current study concentrated on the comparison of the thermo-mechanical characteristics of doped and non-doped $Ba_{0.5}Sr_{0.5}Co_{0.8}Fe_{0.2}O_{3-\delta}$. Although the later material showed higher elastic modulus and fracture strength in absolute values, overall their characteristics mostly agree. It was shown that shortening of the membrane tube from 1 m to half its length should not influence fracture strength significantly. Fractographic analysis ruled out the cutting edge effect in O-ring bending.

Keywords: C. Creep; C. Strength; E. Membranes; Ceramics; Subcritical crack growth

1. Introduction

Mixed ionic–electronic conducting materials are mostly used in industrial applications as electrochemical systems in advanced energy technologies, since they provide high counteractive mobility of ions and electrons. In particular, they are promising for the use as oxygen transport membranes for oxygen separation from ambient air and subsequent supply for combustion in pure oxygen in Oxy-fuel power plants [1,2], as a key component in catalytic membrane reactors [3–5], and as a cathode material in solid oxide fuel cells (SOFCs) [6].

Gas separation is the most promising application for mixed ionic–electronic conductors (MIECs) based on complex oxides with perovskite structure due to their permeation properties. Among these materials, the perovskite $Ba_{0.5}Sr_{0.5}Co_{0.8}Fe_{0.2}O_{3-\delta}$ (BSCF) seems to be the most favorable membrane material since it shows the highest permeation rates [7]. However, on a long term this material appears not to be chemically stable under large oxygen chemical potential gradients (e.g. air/methane) and against CO_2 [8,9] and hence, it can only be used in an Oxy-fuel process if a direct contact with flue gas is avoided [10].

The observed high permeation rates are mainly attributed to oxygen vacancies in the cubic perovskite structure [6], whose amount significantly increases with temperature. However, in order to be economically justified, oxygen transporting membranes (OTMs) and SOFCs should operate at intermediate temperatures between 773 and 1123 K [11]. The permeation rates in this temperature range show a certain degradation which is attributed to a partial phase decomposition of the cubic structure into a hexagonal phase [12]. According to [8,13], the change of radius and spin state of Co is the main driving force for this phase decomposition. Many scientific studies were performed in order to find a way to eliminate this effect. One promising solution [12] seems to be the partial substitution of B-site cations by fixed-valent cations which counteract the radius decrease during the oxidation to low-spin Co^{3+}. In fact, Yakovlev et al. [14] found that optimal partial substitution to preserve long-term stability of the cubic structure can be achieved by doping with 3 mol % of zirconium, which results in chemical composition $Ba_{0.5}Sr_{0.5}(Co_{0.8}Fe_{0.2})_{0.97}Zr_{0.03}O_{3-\delta}$ (BSCFZ).

*Corresponding author. Tel.: +49 2461 61 5463; fax: +49 2461 61 3699.
E-mail address: g.pecanac@fz-juelich.de (G. Pećanac).

0272-8842/$ - see front matter
http://dx.doi.org/10.1016/j.ceramint.2013.07.086

The aim of the current study is to compare the thermo-mechanical characteristics of BSCF with and without 3 mol% Zr, because these materials should serve as substrates to provide mechanical stability for the membrane structure. Since, depending on the loading and environmental conditions, some ceramic materials have strength degradation with time which is related to subcritical crack growth (SCG) [15], it is necessary not only to investigate the initial strength in inert conditions but also its time dependency under application relevant conditions. This unfavorable effect is important to investigate for the cold ends of tubes in some membrane reactor designs. Therefore, BSCF and BSCFZ were compared based on the microstructure, elastic modulus, fracture strength, SCG sensitivity and creep behavior. In particular, the creep behavior is important for the long term structural stability at application temperatures and has suggested to be an indication of the phase stability of BSCF [16]. Since porosity is known to have a large effect on the mechanical properties, it was taken into account for both compositions.

2. Experimental

2.1. Theory

The fracture strength of brittle materials is commonly described by a two-parameter Weibull distribution [17]. In order to compare strength values of brittle materials, the effective volume needs to be equalized. The closed-form solutions for the effective volumes in ring-on-ring and O-ring tests can be found in [18] and [19], respectively. The correlation for volume defects can be described using the relationship [20]:

$$\frac{\sigma_2}{\sigma_1} = \left(\frac{V_1}{V_2}\right)^{(1/m)} \tag{1}$$

where σ_1 and σ_2 represent the stresses, V_1 and V_2 represent the effective volumes of specimen and component, respectively, and m represents the Weibull modulus. The correlation for area defects takes a similar form just by using areas instead of volumes.

Certain materials in particular environmental conditions such as humidity can exhibit SCG since water molecules can react in vicinity of the crack tip and brake structural bonds of the stressed body. This leads to strength degradation of the material. The effect can be assessed by a bending test, in particular the O-ring test, by measuring the characteristic fracture strength σ_0 as a function of stress rate $\dot{\sigma}$ using the equation from [21]. The level of sensitivity to SCG is determined by the n_{SCG} parameter, which is indicated in the strength–stress rate logarithmic plot. Results for dense BSCF [22] obtained with the ring-on-ring test suggest that this material is not strongly affected by SCG.

Detailed theoretical background and governing equations related to the fracture statistics and SCG analysis can be found in [22], where the procedure and results for porous and dense BSCF are also presented. A detailed description of the ring-on-ring test, the testing method used for BSCF characterization, can be found in [23].

2.2. Specimens preparation

The results of BSCF material have been published in [24], where the description of the preparation of BSCF specimens can be also found. Contrary to the tubular specimen geometry of BSCFZ specimens, BSCF specimens were circular plates. However, similar effective volume was taken when comparing the characteristic fracture strength.

Zr-doped BSCFZ powder was delivered by Treibacher Industrie AG Austria (TIAG). The powder was prepared by mixed oxide route using earth alkaline carbonates and oxides of iron and cobalt. It consisted of a pure cubic perovskite phase. The average particle size amounted in 1.6 μm for the fine BSCFZ powder and 45.1 μm for the coarse BSCFZ powder, accompanied by a specific surface area of 1.80 m^2/g and 0.17 m^2/g, respectively. Porous and dense BSCFZ tubes were prepared by stiff-plastic extrusion of ceramic powders. Dense BSCFZ tubes were made by using fine powder. Porous BSCFZ tubes were manufactured by mixing 70 wt% coarse powder and 30 wt% fine powder. Hydroxypropylmethylcellulose by DOW Chemical was used as binder together with methylhydroxypropylcellulose produced by HERCULES. The powder and the binder were mixed with water using a BRABENDER® Plasti-Corder® Lab-Station7 equipped with a mixer type 350. The mixed batches were extruded into tubes using a BRABENDER® Plasti-Corder® Lab-Station7 extruder cascade together with an extrusion die characterized by an outer diameter of 12.25 mm and an inner diameter of 9.75 mm. The extruded tubes were dried at ambient conditions for 24 h. Sintering was carried out at 1130 °C applying a dwell time of 2 h.

2.3. Mechanical testing procedure

2.3.1. O-ring tests

Tests carried out in O-ring bending on an Instron 1362 machine were conducted from room temperature till 800 °C in ambient air. The specimen's displacement was indirectly measured by three equidistant sensors at a radial angle of 60° which measured the relative movement of the loading and supporting plate. The sensors were attached to a ceramic extension rod connected to a linear variable differential transformer (Sangamo, LVDT, range ±1 mm, precision 1.25 μm). The load was determined with a 1.5 kN load cell (Interface 1210 BLR). The temperature was measured by a thermocouple type K which was placed close to the specimen. A detailed summary of performed tests can be found in Table 1.

According to [25], the elastic modulus E in the O-ring test can be calculated as:

$$E = \frac{Fr^2}{dbhe}\left\{\frac{\pi}{4} - \frac{2}{\pi}\left(1-\frac{e^2}{r^2}\right) + 2\frac{e}{r}\left[\frac{2}{\pi}\left(1-\frac{e}{r}\right) - \frac{\pi}{8}\right] + 1.9(1+\upsilon)\frac{e}{r}\right\} \tag{2}$$

Table 1
Description of performed tests obtained in this study.

Material	Test purpose	Temperature [°C]	Number of specimens	Loading rate [N/min]	Outer diameter/inner diameter/width [mm^3]
Dense BSCFZ	Elastic modulus, strength, SCG	22	4	1	8/10/10
			10	100	
			5	1000	
Porous BSCFZ	Elastic modulus, strength	22	26	100	
Dense BSCFZ	Edge effect	22	4	100	
			4	100	8/10/6
Dense BSCFZ	SCG at elevated temperature	600	5	10	8/10/10
			5	100	
Dense BSCFZ	Elastic modulus, strength—as a function of temperature	400	3	100	
		800	6	100	
Dense BSCFZ	Creep	750–950	1	100	8/10/20

where F and d are the force and the deflection, respectively, determined from the linear part of the load-deflection curve, r, b and h are the specimen's middle radius, the width and the wall thickness, respectively, υ is the Poisson's ratio, and e is the distance from the neutral axis. Further details on the test method can be found in [25]. The Poisson ratio was assumed to be 0.3, which is an average value for ceramic materials.

A typical stress distribution of specimen tested in the O-ring test is illustrated in Fig. 1. Although the tensile stresses appear at two vertical positions (marked in Fig. 1 with A, inner wall side on position of contacts between the specimen and the loading and supporting plates) and two horizontal positions (marked in Fig. 1 with B, outer wall side), the stresses at the A-line are significantly higher, therefore the fracture stress analysis concentrated on these positions. The linear bending theory of beams was used to determine the fracture stress since brittle ceramic materials usually fail after elastic deformation. The fracture stress was therefore calculated according to [25]:

$$\sigma = M\frac{h/2-e}{bhe\left(r-\left(h/2\right)\right)} \tag{3}$$

where M is the bending moment. The fracture stress data σ were used to numerically determine the characteristic strength σ_0 and the Weibull modulus m using the maximum likelihood method [26], according to ASTM C1239-07.

2.3.2. Compression tests

The creep behavior was assessed with compression creep tests carried out on an Instron 1362 machine in the temperature range 750–950 °C in ambient air. The tubular specimens were uniaxially loaded between the two supports. The specimens were heated in a load-free state with a heating rate of 8 K/min. The applied stress was 63 MPa. The strain was calculated from the measured deformation by:

$$\varepsilon = \Delta h/h_0 \tag{4}$$

where h_0 is the initial height and Δh is the specimen's deflection. The Arrhenius approach [27] was used to determine the creep rate $\dot{\varepsilon}$ based on Norton's law [28]:

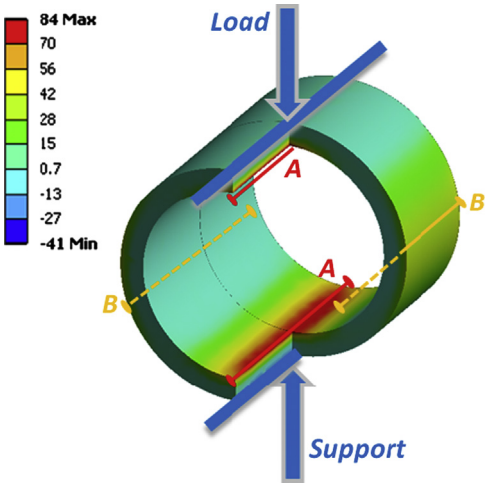

Fig. 1. Cross-section revealing typical distribution of maximum principle stresses in an O-ring test with indicative critical positions of tensile stresses.

$$\dot{\varepsilon} = A\,\sigma^n \exp\left(-\frac{Q}{R\,T}\right) \tag{5}$$

where A and n are the constants, Q is the activation energy, R is the universal gas constant and T is the temperature.

The flatness of the previously ground and polished base surfaces and the parallelism was ensured to be 0.04 mm and 0.1 mm, respectively, to minimize surface effects and superimposed bending induced by misalignments. The vertical displacement of the specimens was indirectly determined by a sensor in the central axis of a tubular specimen, which measured the relative movement of the loading and supporting plate. The load was measured by load cells with a 10 kN range (1210 ACK, Interface Company). Otherwise, the measurements and used devices were similar as in the case of the O-ring test.

3. Results and discussions

3.1. Microstructure

Microstructural images of the investigated and reference material in the nominal dense state are compared in Fig. 2. These images confirm more homogeneous structure of BSCF with spherical pores of similar size (Fig. 2a), while in the microstructure of the dense BSCFZ (Fig. 2b) a certain amount of larger pores is present. Hence, images obtained at larger magnification verify that porous BSCF has a very homogeneous microstructure with spherical pores (Fig. 3a and b), whereas porous BSCFZ has an inhomogeneous pore structure with sharp irregular edges (Fig. 4). Since the specimens were produced by an extrusion process, it was also necessary to compare the cross-section in the transversal and longitudinal direction. As can be seen in Fig. 4, there is no anisotropy, gradient or microstructural difference in both directions.

The microstructural results are compiled in Table 2. The grain size analysis showed larger values for dense BSCFZ, however, the porosities of the materials are rather similar for both materials comparing the respective dense and porous states. The grain sizes of porous specimens are assumed to be similar to their dense counterparts, since similar average grain size has been determined for dense and porous BSCF [29]. In case of porous BSCFZ, the standard deviation would be very high due to microstructural inhomogeneities which would not give any conclusive result.

3.2. Mechanical properties

Room temperature mechanical characterization results and literature data are compiled in Table 2 along with their characteristic parameters. Although the elastic modulus seems similar for the dense materials, the porosity needs to be taken into account accurately since it has a larger effect for dense materials. The conclusion is straightforward by observing Fig. 5. Porous and dense BSCF data found in literature [24,29,30] showed ~two times higher elastic moduli than BSCFZ for the entire porosity range. A higher elastic modulus is sometimes an advantage since it leads to smaller deformation, but it can also be a disadvantage since it leads to higher stresses for a particular strain state. The temperature dependence of elastic modulus for dense materials is shown in Fig. 6, where the data for BSCF are taken from [30]. The values for dense BSCF are higher, implying an effect of the processing parameters. Since the current work concentrates on room and operational temperatures, it was not attempted to confirm the local minimum at around 200 °C.

Fracture stresses were analyzed statistically to determine the characteristic fracture strength and the Weibull modulus at different loading rates. Fracture strengths showed a similar behavior as the elastic moduli (Table 2 and Fig. 5). Note that, since investigations were based on different testing methods, the tested effective volumes were not similar. For direct comparison, the strength data were normalized with respect to the effective volumes using Eq. (1) since the Weibull theory

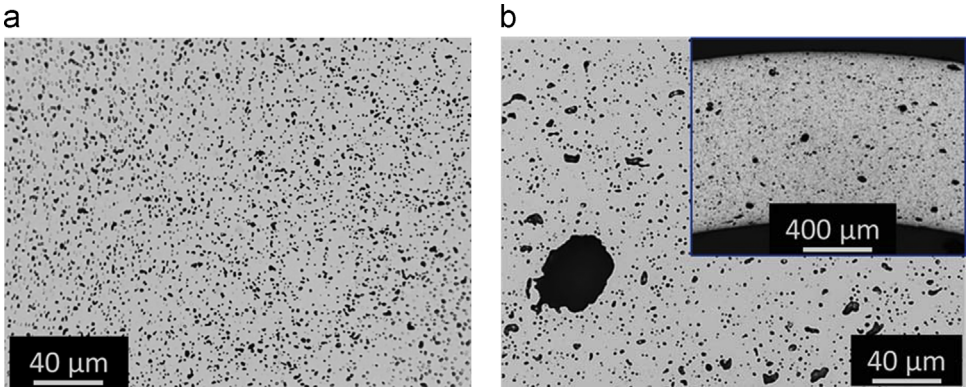

Fig. 2. Microstructural images of the (a) dense reference material BSCF, and (b) investigated dense BSCFZ material.

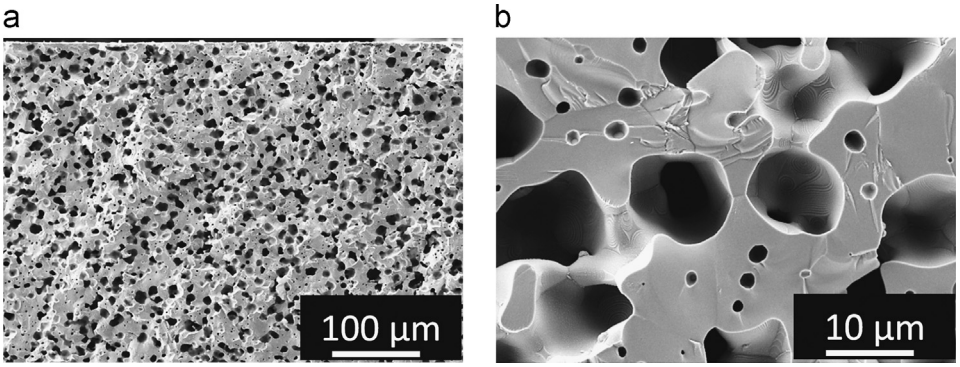

Fig. 3. Homogeneous microstructure of porous BSCF (a) containing spherical pores (b).

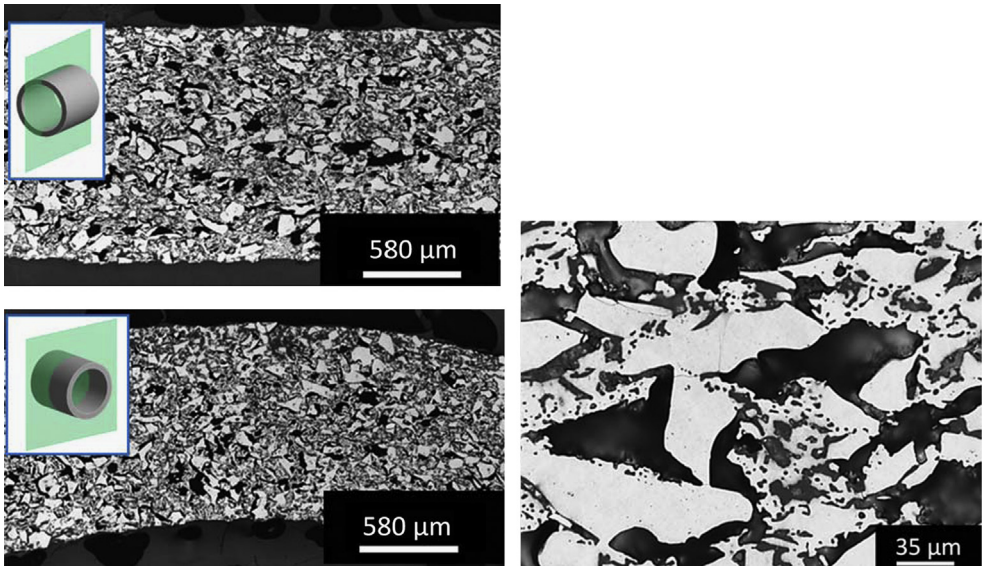

Fig. 4. Inhomogeneous microstructure of porous BSCFZ containing sharp pores. No porosity or any other physical gradient was found in the longitudinal or transversal direction of extrusion which might lead to anisotropic properties.

Table 2
Comparison of mechanical properties with their dependent parameters for the investigated and reference material.

Material	Dense BSCF	Dense BSCFZ	Porous BSCF	Porous BSCFZ
Porosity [%]	9 ± 1	6 ± 0.1	34 ± 2	38 ± 2
Grain size [µm]	7 ± 3	20 ± 8	–	–
Elastic modulus [GPa]	52 ± 1	50 ± 3	35 ± 3	15 ± 2
Characteristic fracture strength [MPa]	86 ± 4	84 ± 4	31 ± 1	18 ± 1
Unbiased Weibull modulus	7 ± 2	7 ± 2	8 ± 3	7 ± 1
Performed test	Ring-on-ring	O-ring	Ring-on-ring	O-ring
Effective volume [mm^3]	3.5	0.8	5.2	0.9

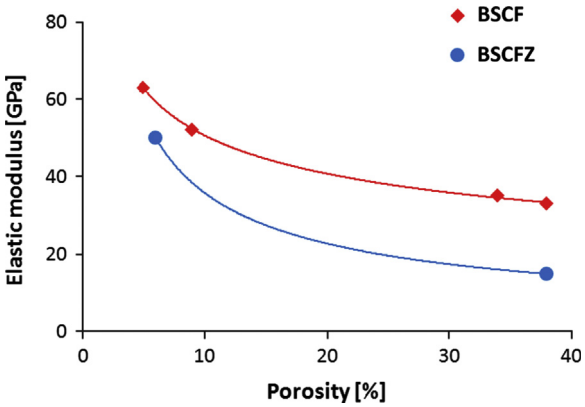

Fig. 5. Porosity dependence of elastic modulus for BSCFZ. The literature data for BSCF [24,29,30] are compiled and also shown in plot. The comparison indicates higher elastic modulus of the reference material.

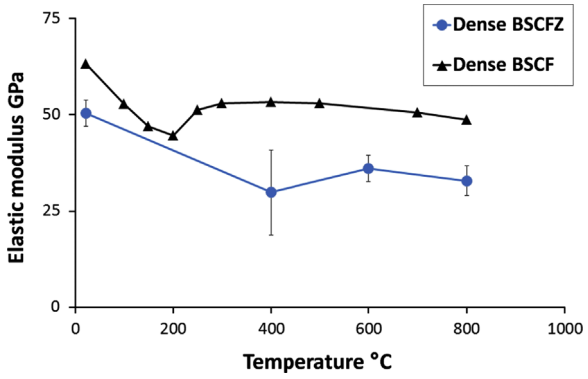

Fig. 6. Temperature dependence of elastic moduli revealing similar behavior. Elastic modulus of BSCF was taken from the literature [30].

of flaw distribution indicates that larger volume leads to lower strength. As a reference point, an effective volume of 28,000 mm^3 was used based on a realistic tubular design with the dimensions $\varnothing_{inside}8/\varnothing_{outside}10 \times 1000$ mm^3. Depending on the performed test, the specimens had effective volumes from 0.8 mm^3 up to 5 mm^3. The resulting curves in Fig. 7 clearly illustrate that the strength is significantly lower for the longer membrane tube compared to the small test specimens. Nevertheless, the strength ratios remained almost the same. Interestingly, a reduction of the tube length by 50% would not lead to a substantial increase of the strength, since the effective volume is still in the plateau region of the logarithmic curve.

Fracture stresses of dense BSCFZ were also investigated as a function of temperature (Fig. 8). As in the case of BSCF, this material showed the same tendency although with a lower

absolute values than in the previous study on BSCF [30]. The strength of BSCFZ reveals a decreasing tendency above 600 °C compared to BSCF, which is assumed to be a result of large scattering (two specimens showed extremely lower fracture stress) and not typical material's behavior. Since porous and dense BSCF verified similar temperature-dependent strengths [29,30], a similar effect can be assumed for porous and dense BSCFZ.

BSCFZ specimens were tested in an O-ring geometry, in which the determined fracture stress might be influenced by an edge effect associated with the specimen's cutting. Hence, a study was performed on the same batch of dense BSCFZ by comparing the average fracture stress of tubular specimens with different lengths of 10 mm and 6 mm, respectively. The increase of the average strength from 94 MPa to 104 MPa by reducing the effective volume indicated that the specimen did not fail due to an edge quality, but from flaws in the microstructure, confirming that there is no influence of an edge effect in case of dense BSCFZ in the O-ring test. An analysis of these data based on Eq. (1) also confirmed the dependence on the effective volume, since the calculation differs only by 3% from the experimentally measured fracture stress.

3.3. Subcritical crack growth

The graphical representation of the characteristic fracture strengths as a function of loading rate at RT and 600 °C is given in Fig. 9. According to [21], critical values of the n_{SCG} parameter are around 20 and below. The values obtained for BSCFZ at RT (n_{SCG}~250) and at 600 °C (almost horizontal line in plot→infinite n_{SCG}) reveal a negligible influence on this material in both cases. In comparison with porous and dense BSCF [24], a slight SCG sensitivity of BSCF was found, especially for the dense state. Due to the usual statistical distribution of the results for brittle materials, and the experimental uncertainty, it is difficult to conclude if Zr doping influences the SCG sensitivity. According to [24], porous BSCFZ should be even more insensitive due to the fact that pores frequently act as crack propagation inhibitors.

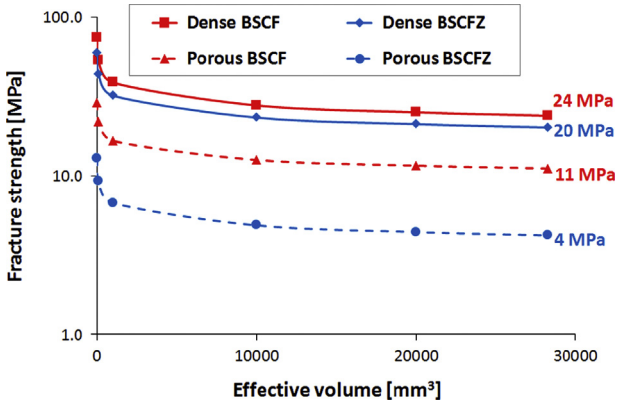

Fig. 7. Fracture strength as a function of effective volume. A decrease of the membrane tube from 1 m to half its length would not lead to a significant strength increase.

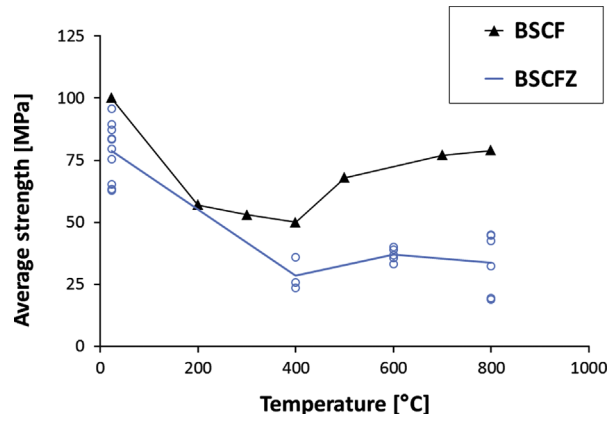

Fig. 8. Fracture stresses as a function of temperature revealing similar behavior of BSCFZ and BSCF [30]. A decrease after 600 °C for BSCFZ might be a result of large scatter in the data.

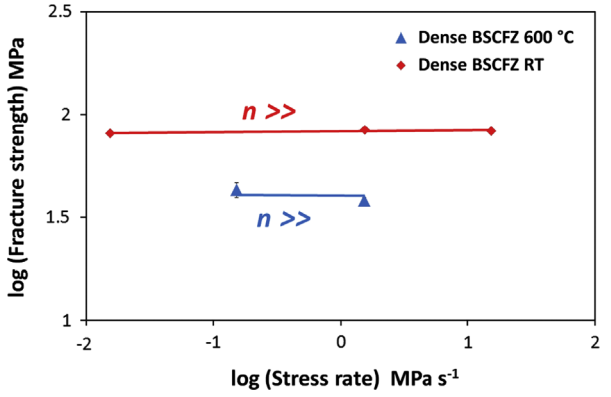

Fig. 9. Subcritical crack growth analysis revealing low influence on BSCFZ at RT and at 600 °C.

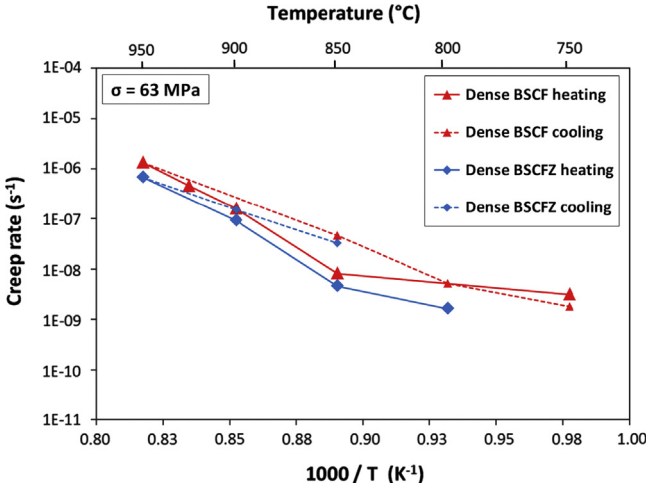

Fig. 10. Creep rates of BSCF [31] and BSCFZ at an applied stress of 63 MPa. The hysteresis effect associated with the existence of hexagonal phase is present for both materials.

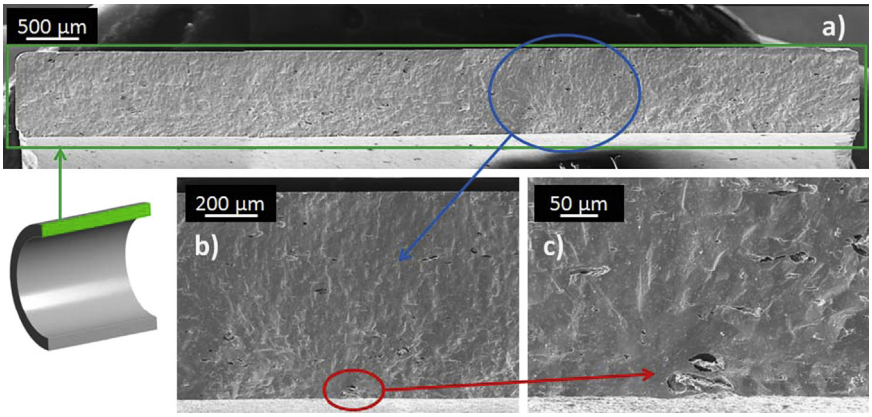

Fig. 11. Large pores, typical failure origins of BSCFZ material, verified that this material fails from the production imperfection and the fracture strength is not biased by the cutting edge effect in an O-ring test.

3.4. Creep behavior

The creep behavior of BSCF was verified to have a hysteresis effect associated with the existence of a hexagonal phase [31]. This phase is not favorable since it decreases the permeation rates. However, it seems to be able to decrease the creep deformation. Accordingly, it is apparently favorable from a mechanical point of view. The creep deformation was measured here for dense BSCFZ to assess the doping influence. The resulting curves are shown in Fig. 10. The tests were performed at 63 MPa and the values were compared to BSCF data [31]. The creep deformation of BSCFZ is slightly lower, which might be associated with the larger grain size, since the creep mechanism in case of BSCF(Z) is supposed to be a diffusional creep, whose magnitude depends directly on the grain size. Therefore, both materials should have similar creep rates for comparable grain sizes, implying that the Zr doping does not affect the creep deformation. In comparison with other potential membrane materials [32] with respect to creep behavior, this material confirms its good characteristics in a membrane application.

3.5. Fractography

BSCF is known to fail from volume defects [22]. Fractographic analysis revealed that BSCFZ has large failure relevant pores, verifying the use of effective volumes [19] (Eq. (1)) to analyze the strength behavior of larger components. Furthermore, the analysis again verified that the edge effect in the O-ring test can be ruled out in case of BSCFZ. Typical position of failure origin is shown in Fig. 11a, confirming that the fracture of specimen was not initiated on the cut edge from artificial flaws induced by tube cutting but from a microstructural defect in the inner part of the tubular specimen. Fig. 11b shows the fracture origin in higher magnification with visible radial cracking directions and Fig. 11c verifies a pore as a failure origin. This large pore on the critical position A (highest tensile stress, defined in Fig. 1) acted as a stress concentrator and led to a failure of the specimen.

4. Conclusions

Thermo-mechanical characteristics of BSCFZ are assessed and compared to BSCF data. The microstructure of BSCF seems to be more homogeneous, which is reflected in higher fracture strength. It might be associated with differences in production procedures and not an effect of the Zr doping. Due to a saturation of the strength-effective volume dependence, shortening of the membrane tubes from 1 m to half its length should not influence fracture strengths significantly. Elastic moduli and fracture strengths of BSCFZ showed similar temperature dependencies with lower absolute values. BSCFZ revealed slightly lower sensitivity to SCG, but it is difficult to claim whether Zr influences the level of subcritical crack growth. The creep deformation was found to be similar for both materials. Fractographic analysis verified large pores as failure origins and additionally ruled out the cutting edge effect for testing BSCFZ in O-ring bending. The difference in mechanical properties of BSCF and BSCFZ is most likely a result of different production procedures, which is also reflected in the microstructure, and not necessarily induced by the Zr doping. Although BSCFZ shows lower elastic modulus and fracture strength, it can be overall concluded that thermo-mechanical characteristics of BSCF and BSCFZ mostly agree.

Acknowledgments

The investigations presented in this work are funded by the European Union through the HETMOC FP7 Project under the theme: Energy.2010.6.1-1. The authors would like to express their gratitude to Ms. T. Osipova, Mr. R. Küppers and Mr. J. Mönch for the experimental support, and Dr. E. Wessel and Dr. D. Grüner for the SEM analyses.

References

[1] J.F. Vente, W.G. Haije, Z.S. Rak, Performance of functional perovskite membranes for oxygen production, Journal of Membrane Science 276 (2006) 178–184.

[2] I. Pfaff, A. Kather, Comparative thermodynamic analysis and integration issues of CCS steam power plants based on oxy-combustion with cryogenic or membrane based air separation, Energy Procedia 1 (2009) 495–502.
[3] H.J.M. Bouwmeester, Dense ceramic membranes for methane conversion, Catalysis Today 82 (2003) 141–150.
[4] L. Olivier, S. Haag, C. Mirodatos, A.C. van Veen, Oxidative coupling of methane using catalyst modified dense perovskite membrane reactors, Catalysis Today 142 (2009) 34–41.
[5] F.T. Akin, Y.S. Lin, Controlled oxidative coupling of methane by ionic conducting ceramic membrane, Catalysis Letters 78 (2002) 239–242.
[6] Z. Shao, S.M. Haile, A high-performance cathode for the next generation of solid-oxide fuel cells, Nature 431 (2004) 170–173.
[7] S. Baumann, J.M. Serra, M.P. Lobera, S. Escolástico, F. Schulze-Küppers, W.A. Meulenberg, Ultrahigh oxygen permeation flux through supported $Ba_{0.5}Sr_{0.5}Co_{0.8}Fe_{0.2}O_{3-\delta}$ membranes, Journal of Membrane Science 377 (2011) 198–205.
[8] M. Arnold, H. Wang, A. Feldhoff, Influence of CO_2 on the oxygen permeation performance and the microstructure of perovskite-type $(Ba_{0.5}Sr_{0.5})(Co_{0.8}Fe_{0.2})O_{3-\delta}$ membranes, Journal of Membrane Science 293 (2007) 44–52.
[9] H.J.M. Bouwmeester, A.J. Burggraaf, Dense ceramic membranes for oxygen separation, in: A.J. Burggraaf, L. Cot (Eds.), Membrane Science and Technology, Elsevier, 1996, pp. 435–528 (Chapter 10).
[10] R. Kneer, D. Toporov, M. Forster, D. Christ, C. Broeckmann, E. Pfaff, M. Zwick, S. Engels, M. Modigell, OXYCOAL-AC: towards an integrated coal-fired power plant process with ion transport membrane-based oxygen supply, Energy and Environmental Science 3 (2010) 198–207.
[11] O. Ravkina, T. Klande, A. Feldhoff, Investigation of Zr-doped BSCF perovskite membrane for oxygen separation in the intermediate temperature range, Journal of Solid State Chemistry 201, 2013, 101–106.
[12] S. Švarcová, K. Wiik, J. Tolchard, H.J.M. Bouwmeester, T. Grande, Structural instability of cubic perovskite $Ba_xSr_{1-x}Co_{1-y}FeyO_{3-d}$, Solid State Ionics 178 (2008) 1787–1791.
[13] K. Efimov, Q. Xu, A. Feldhoff, Transmission electron microscopy study of $Ba_{0.5}Sr_{0.5}Co_{0.8}Fe_{0.2}O_{3-\delta}$ perovskite decomposition at intermediate temperatures, Chemistry of Materials 22 (2010) 5866–5875.
[14] S. Yakovlev, C.Y. Yoo, S. Fang, H.J.M. Bouwmeester, Phase transformation and oxygen equilibration kinetics of pure and Zr-doped $Ba_{0.5}Sr_{0.5}Co_{0.8}Fe_{0.2}O_{3-\delta}$ perovskite oxide probed by electrical conductivity relaxation, Applied Physics Letters 96 (2010).
[15] S.M. Wiederhorn, Influence of water vapor on crack propagation in soda-lime glass, Journal of the American Ceramic Society 50 (1967) 407–414.
[16] B. Rutkowski, J. Malzbender, R.W. Steinbrech, T. Beck, H.J.M. Bouwmeester, Influence of thermal history on the cubic-to-hexagonal phase transformation and creep behaviour of $Ba_{0.5}Sr_{0.5}Co_{0.8}Fe_{0.2}O_{3-\delta}$ ceramics, Journal of Membrane Science 381 (2011) 221–225.
[17] W. Weibull, A statistical distribution function of wide applicability, Journal of Applied Mechanics 18 (1951) 293–297.
[18] J.A. Salem, L. Powers, Guidelines for the testing of plates, in: Proceedings of the 27th Annual Cocoa Beach Conference on Advanced Ceramics and Composites: B, Ceramic Engineering and Science Proceedings, 2008, John Wiley & Sons, Inc., pp. 357–364.
[19] M.O. Jadaan, L.D. Shelleman, C.J. Conway, J.J. Mecholsky, E.R. Tressler, Prediction of the strength of ceramic tubular components. I, analysis, Journal of Testing and Evaluation 19 (1991) 181–191.
[20] P. Supancic, R. Danzer, S. Witschnig, E. Polaczek, R. Morrell, A new test to determine the tensile strength of brittle balls—the notched ball test, Journal of the European Ceramic Society 29 (2009) 2447–2459.
[21] S.R. Choi, J.A. Salem, F.A. Holland, Estimation of Slow Crack Growth Parameters for Constant Stress-Rate Test Data of Advanced Ceramics and Glass by the Individual Data and Arithmetic Mean Methods, Lewis Research Center, National Aeronautics and Space Administration, 1997.
[22] G. Pećanac, S. Baumann, J. Malzbender, Mechanical properties and lifetime predictions for $Ba_{0.5}Sr_{0.5}Co_{0.8}Fe_{0.2}O_{3-\delta}$ membrane material, Journal of Membrane Science 385–386 (2011) 263–268.
[23] G. Pećanac, T. Bause, J. Malzbender, Ring-on-ring testing of thin, curved bi-layered materials, Journal of the European Ceramic Society 31 (2011) 2037–2042.
[24] G. Pećanac, S. Foghmoes, M. Lipińska-Chwałek, S. Baumann, T. Beck, J. Malzbender, Strength degradation and failure limits of dense and porous ceramic membrane materials, Journal of the European Ceramic Society 33 (2013) 2689–2698.
[25] K. Bongartz, E. Gyarmati, H. Schuster, K. Täuber, The brittle ring test: a method for measuring strength and Young's modulus on coatings of HTR fuel particles, Journal of Nuclear Materials 62 (1976) 123–137.
[26] R.W. Davidge, G. Tappin, Thermal shock and fracture in ceramics, Transactions and Journal of the British Ceramic Society 66 (1967) 405–422.
[27] J.X. Yi, H.L. Lein, T. Grande, S. Yakovlev, H.J.M. Bouwmeester, High-temperature compressive creep behaviour of the perovskite-type oxide $Ba_{0.5}Sr_{0.5}Co_{0.8}Fe_{0.2}O_{3-d}$, Solid State Ionics 180 (2009) 1564–1568.
[28] F.H. Norton, The Creep of Steel at High Temperatures, McGraw-Hill Book Company, Inc., 1929.
[29] M. Lipinska-Chwalek, J. Malzbender, A. Chanda, S. Baumann, R.W. Steinbrech, Mechanical characterization of porous $Ba_{0.5}Sr_{0.5}Co_{0.8}Fe_{0.2}O_{3-d}$, Journal of the European Ceramic Society 31 (2011) 2997–3002.
[30] B.X. Huang, J. Malzbender, R.W. Steinbrech, L. Singheiser, Discussion of the complex thermo-mechanical behavior of $Ba_{0.5}Sr_{0.5}Co_{0.8}Fe_{0.2}O_{3-\delta}$, Journal of Membrane Science 359 (2010) 80–85.
[31] B. Rutkowski, J. Malzbender, T. Beck, R.W. Steinbrech, L. Singheiser, Creep behaviour of tubular $Ba_{0.5}Sr_{0.5}Co_{0.8}Fe_{0.2}O_{3-\delta}$ gas separation membranes, Journal of the European Ceramic Society 31 (2011) 493–499.
[32] M. Lipińska-Chwałek, G. Pećanac, J. Malzbender, Creep behaviour of membrane and substrate materials for oxygen separation units, Journal of the European Ceramic Society 33 (2013) 1841–1848.